

Constraints on global mean sea level during Pliocene warmth

Oana A. Dumitru^{1,6}, Jacqueline Austermann^{2,6}, Victor J. Polyak³, Joan J. Fornós⁴, Yemane Asmerom³, Joaquín Ginés⁴, Angel Ginés⁴ & Bogdan P. Onac^{1,5*}

Reconstructing the evolution of sea level during past warmer epochs such as the Pliocene provides insight into the response of sea level and ice sheets to prolonged warming¹. Although estimates of the global mean sea level (GMSL) during this time do exist, they vary by several tens of metres^{2–4}, hindering the assessment of past and future ice-sheet stability. Here we show that during the mid-Piacenzian Warm Period, which was on average two to three degrees Celsius warmer than the pre-industrial period⁵, the GMSL was about 16.2 metres higher than today owing to global ice-volume changes, and around 17.4 metres when thermal expansion of the oceans is included. During the even warmer Pliocene Climatic Optimum (about four degrees Celsius warmer than pre-industrial levels)⁶, our results show that the GMSL was 23.5 metres above the present level, with an additional 1.6 metres from thermal expansion. We provide six GMSL data points, ranging from 4.39 to 3.27 million years ago, that are based on phreatic overgrowths on speleothems from the western Mediterranean (Mallorca, Spain). This record is unique owing to its clear relationship to sea level, its reliable U–Pb ages and its long timespan, which allows us to quantify uncertainties on potential uplift. Our data indicate that ice sheets are very sensitive to warming and provide important calibration targets for future ice-sheet models⁷.

Accurate predictions of future sea-level change hinge on our understanding of how ice sheets respond to changes in global temperature. To understand ice-sheet stability under prolonged warming (such as if the current level of temperature increase continues), we can use reconstructed sea level during past periods when Earth's climate was warmer than today¹. The Pliocene epoch (5.33 to 2.58 million years ago, Ma) was the most recent extended global warm period immediately preceding the inception of the high-magnitude glacial/interglacial variations of the Pleistocene⁸. The mid-Piacenzian Warm Period (MPWP), an interval during the Late Pliocene (3.264 to 3.025 Ma), has been used as an analogue for future anthropogenic warming since atmospheric CO₂ conditions were comparable to present-day values (~400 ppm)⁹ and estimated global mean temperatures were elevated by 2–3 °C relative to the pre-industrial period⁵.

Oxygen isotope ratios from benthic foraminifera¹⁰ paired with deep ocean temperature estimates have been used to approximate ice-volume-equivalent GMSL changes over the Pliocene^{11,12}. While invaluable, these approaches are limited by uncertainties in the methodology and a number of factors (for example, post-burial diagenesis, long-term changes in seawater chemistry and salinity) that are poorly constrained and may bias the sea-level estimates³. Field mapping of palaeoshorelines has been a complementary approach and has provided several local reconstructions of Pliocene sea level¹³. Local estimates also exist for the Strait of Gibraltar, where they are based on the marginal basin residence time method and measurements of planktonic foraminifera². Local estimates of sea level can vary considerably from the GMSL owing to processes such as glacial isostatic adjustment (GIA)¹⁴ and dynamic topography¹⁵, which can be corrected for, but have substantial

uncertainties. Lastly, GMSL estimates have also been derived from climatically driven ice-sheet simulations^{4,7,16}, but these vary notably as a result of model uncertainties. All these challenges have led to considerable disagreement between estimates of the GMSL during the MPWP, with values ranging from about 10 m to over 50 m above present sea level (m.a.p.s.l.)^{1,2,12,17,18}. This disparity hinders the assessment of past and future ice-sheet stability⁷.

Here we present Pliocene sea-level data from Coves d'Artà in the western Mediterranean (Mallorca, Spain; Fig. 1a, b) that are based on U–Pb absolute-dated phreatic overgrowths on speleothems (POS). POS offer several important benefits over other Pliocene sea-level indicators since they store all information needed for a meaningful sea-level index point: (1) precise spatial geographic positioning, (2) accurate elevation, (3) clear indicative meaning (their growth covers the full tidal range, thus having an explicit relation to past sea level; see Methods), and (4) an absolute age (since the crystalline aragonite/calcite often contains suitable uranium concentrations for robust dating¹⁹). POS are primarily precipitated in caves, at the water/air interface as CO₂ degasses from brackish cave pools. The water table in these caves is, and was in the past, coincident with sea level, given that the caves are at most 300 m away from the coast and the karst topography is low. Six POS levels have been identified at elevations from 22.6 to 31.8 m.a.p.s.l. (uncertainties in the elevation measurement and the indicative range are less than 1 m; Fig. 1c, Table 1). We interpret these levels as still stands, that is, corresponding to periods of time during which sea level has been stable long enough to allow the precipitation of carbonate overgrowths. This could occur during a sea-level highstand, lowstand or intermediate stand. The palaeo sea level still stands are distinctly delineated by POS that occur either as overgrowths covering cave walls and pre-existing flowstones (top and bottom insets of Fig. 1d) or as standalone structures on stalactites and stalagmites (middle inset of Fig. 1d). Based on 70 U–Pb analyses, the geochronology of these POS yielded ages between 4.39 ± 0.39 Ma and 3.27 ± 0.12 Ma (Table 1; see Methods). These are unique because radiometric-dated records of Pliocene sea level are entirely independent of orbitally tuned chronologies.

To infer the GMSL from these local observations, the POS elevations are corrected for GIA, which is the viscoelastic adjustment of the solid Earth, its gravity field, and rotation axis to changes in the ice and ocean load. The GIA correction is the deviation of local sea level from the global mean and we calculate this correction using a gravitationally self-consistent sea-level formulation²⁰ paired with three GMSL scenarios^{2,4,10} and a suite of viscoelastic Earth structures (see Methods). To calculate the GMSL we assume a fixed oceanic area and consider total ice-volume change, not only ice above the flotation level. Long-term deformation at passive margins due to sediment loading²¹ or dynamic topography¹⁵ can further contribute to local sea-level changes. Since model predictions of these processes have high uncertainties, we estimate bounds on the long-term deformation from sea-level indicators during Marine Isotope Stage (MIS) 5 and the Upper Miocene, as

¹Karst Research Group, School of Geosciences, University of South Florida, Tampa, FL, USA. ²Department of Earth and Environmental Sciences, Columbia University, Lamont-Doherty Earth Observatory, Palisade, NY, USA. ³Department of Earth and Planetary Sciences, University of New Mexico, Albuquerque, NM, USA. ⁴Earth Sciences Research Group, Universitat de les Illes Balears, Palma, Spain. ⁵Department of Geology, Babeş-Bolyai University, Cluj-Napoca, Romania. ⁶These authors contributed equally: Oana A. Dumitru, Jacqueline Austermann. *e-mail: bonac@usf.edu

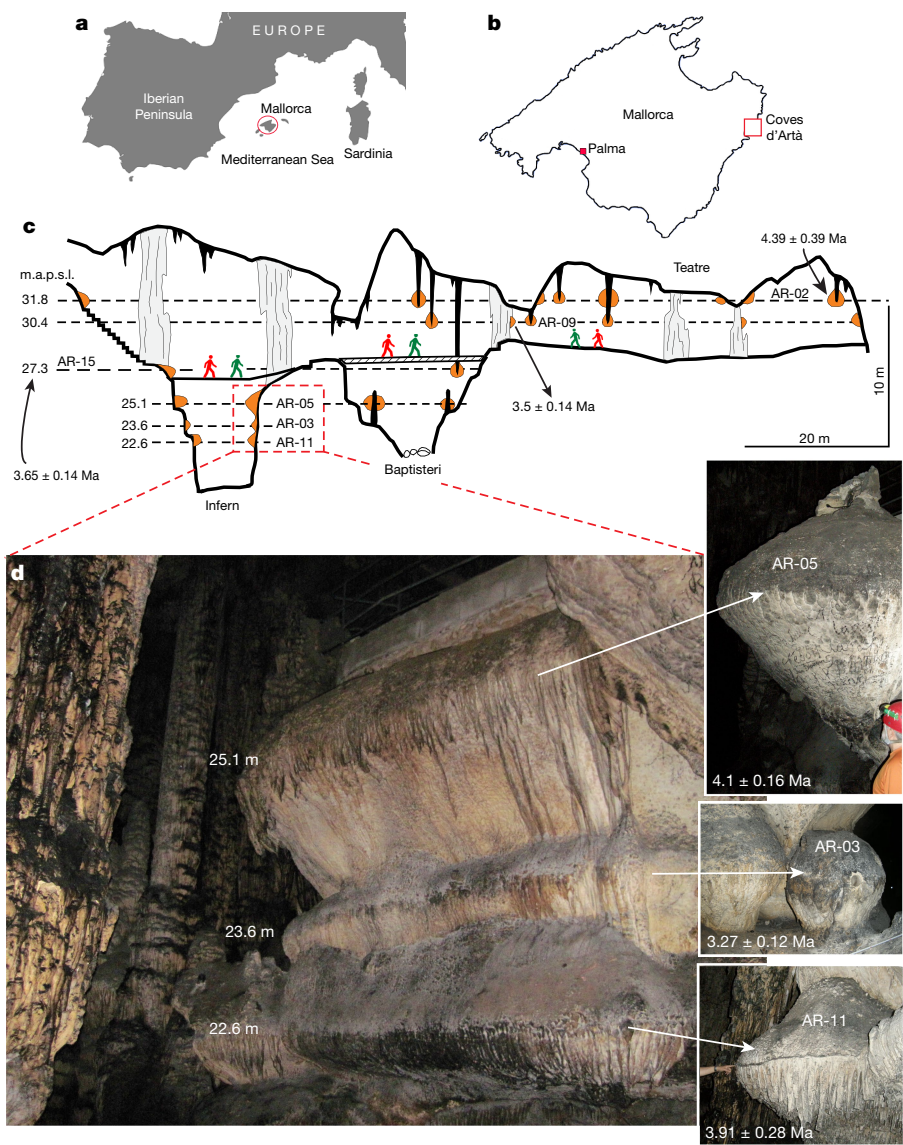


Fig. 1 | POS in Coves d'Artà. **a**, Map showing Mallorca (red circle) in the western Mediterranean. **b**, Location of Coves d'Artà on the island. **c**, Longitudinal profile through the lower section of the cave showing the present-day elevation and ages of the six POS horizons and the sampling sites. **d**, POS at three elevations within the Infern Room with close-up views (insets). Maps (**a**, **b**) are available under CC Public Domain License from <https://pixabay.com/illustrations/map-europe-world-earth-continent-2672639/> and <https://pixabay.com/illustrations/mallorca-map-land-country-europe-968363/>, respectively.

well as a comparison between the relative elevations of the six POS and the GMSL change from three GMSL curves (see Methods). To assess the GMSL we account for uncertainties in the elevation measurement and the indicative range, and correct for GIA, long-term uplift, and thermal expansion (Fig. 2, Table 1; see Methods). Because we correct for thermal expansion, our GMSL estimates throughout the text are sea-level-equivalent ice-volume changes. For better comparison with published estimates, Table 1 additionally includes GMSL estimates without the correction for thermal expansion. Applying all corrections results in a non-Gaussian distribution for our reconstructed GMSL,

of which we report the mode (that is, the most likely value) as our best estimate and in parentheses the 16th and 84th percentiles as our uncertainty range. Each POS-derived sea-level still stand and the temporally coincident major climatic events evidenced in either marine or terrestrial records are discussed in chronological order and reported in Table 1. The oldest sample (AR-02 at 4.39 ± 0.39 Ma) yields a GMSL estimate of 23.5 m.a.p.s.l. (9.0–26.7 m.a.p.s.l.). Its growth is coincident with an interval considered to be probably the warmest during the Pliocene (~4.4–4.0 Ma, the Pliocene Climatic Optimum), with global mean

Table 1 | Sample information and results

Sample code	Sample elevation (m.a.p.s.l.)	Indicative range (m)	Age (Myr)	Sample mineralogy	Maximum thickness (m)	GIA correction (m)	Uplift correction (m)	Thermal expansion correction (m)	GMSL (m.a.p.s.l.)	GMSL without correction for thermal expansion (m.a.p.s.l.)
AR-02	31.8 ± 0.25	0.55	4.39 ± 0.39	Calcite	0.20	1.3 ± 3.1	9.0 (2.5–19.4)	1.6 ± 0.6	23.5 (9.0–26.7)	25.1 (10.6–28.3)
AR-05	25.1 ± 0.25	1.20	4.10 ± 0.16	Aragonite	0.80	1.5 ± 3.1	8.4 (2.3–18.2)	1.5 ± 0.5	16.9 (3.5–20.2)	18.4 (4.9–21.6)
AR-11	22.6 ± 0.25	0.85	3.91 ± 0.28	Calcite	0.50	1.4 ± 3.1	8.0 (2.2–17.3)	1.4 ± 0.5	14.7 (2.0–18.0)	16.1 (3.4–19.4)
AR-15	27.3 ± 0.25	0.50	3.65 ± 0.14	Aragonite	0.25	1.7 ± 2.9	7.4 (2.1–16.2)	1.3 ± 0.5	19.5 (7.6–22.6)	20.8 (8.9–23.9)
AR-09	30.4 ± 0.25	0.70	3.50 ± 0.14	Aragonite	0.40	1.9 ± 2.9	7.1 (2.0–15.5)	1.2 ± 0.4	22.5 (11.3–25.7)	23.7 (12.5–27.0)
AR-03	23.6 ± 0.25	0.55	3.27 ± 0.12	Aragonite	0.30	1.8 ± 2.7	6.7 (1.8–14.5)	1.2 ± 0.4	16.2 (5.6–19.2)	17.4 (6.8–20.3)

The age uncertainties are reported as 2σ absolute values. Uplift correction shows the median value and the 16th and 84th percentiles in parentheses as uncertainty bounds. The GMSL shows the mode and 16th and 84th percentiles in parentheses as uncertainty bounds. The GMSL estimates include a correction for GIA, long-term uplift, and thermal expansion. Uncertainties in these corrections are 1σ . All reported corrections are subtracted from the sample elevation to obtain the GMSL. In the last column we provide GMSL estimates that are corrected only for GIA and long-term uplift, but not for thermal expansion.

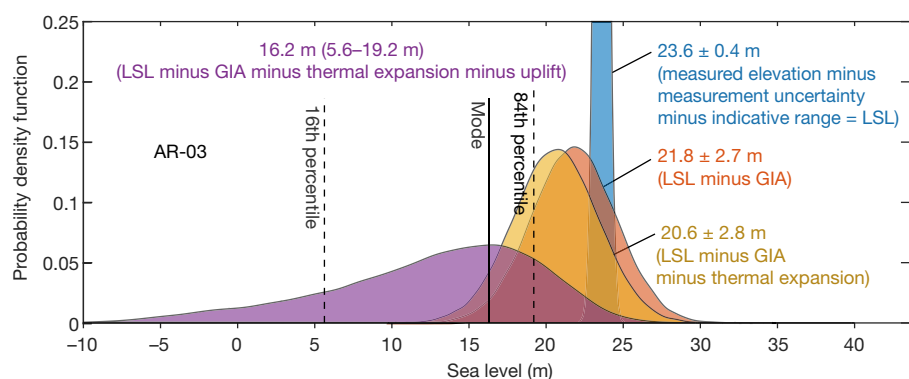


Fig. 2 | GIA and other corrections.

Contribution of different corrections (GIA, uplift and thermal expansion) and uncertainties when inferring the GMSL from the POS elevation (this breakdown is for AR-03; see Extended Data Fig. 8 for all POS). Probability density function of the POS elevation with consecutive corrections for the measurement and indicative range leading to an estimate of local sea level (LSL; blue), GIA (orange), long-term uplift (purple curve) and thermal expansion (yellow). We choose the mode (solid black line) as the best estimate and the 16th and 84th percentiles (dashed black line) as the uncertainty range.

temperatures roughly 4 °C higher than pre-industrial values⁶ and elevated CO₂ (ref. ²²) (Fig. 3a).

A GMSL estimate of 16.9 m.a.p.s.l. (3.5–20.2 m.a.p.s.l.) at 4.1 ± 0.16 Ma is based on a core extracted from AR-05, the thickest POS horizon (top inset in Fig. 1d). A pronounced expansion of the ice sheets (MIS Gi22/Gi20) and the associated sea-level drop was documented at ~4 Ma in several locations in the Northern Hemisphere²³ and in Prydz Bay, Antarctica²⁴. Therefore, AR-05 is interpreted to reflect a rather long, muted sea-level still stand that occurred before this cooler Pliocene interval.

Similarly, the inner part of AR-11 (bottom inset in Fig. 1d), documents a lower GMSL of 14.7 m.a.p.s.l. (2.0–18.0 m.a.p.s.l.) at 3.91 ± 0.28 Ma. Sample AR-15 marks a GMSL of 19.5 m.a.p.s.l. (7.6–22.6 m.a.p.s.l.) at 3.65 ± 0.14 Ma and overlaps with the Northern Hemisphere glacial interval known as MIS MG 12 (~3.7–3.6 Ma), which is considered to represent the Early/Late Pliocene transition^{10,23,25}. Terrestrial and marine data indicate that the Northern Hemisphere glaciation onset was around 3.6 Ma (refs ^{23,25}), but other records from the Northern and Southern hemispheres suggest that relatively warm climatic conditions prevailed until 3.5 Ma (ref. ²⁶). This observation is supported

by the presence of yet another horizon formed in Coves d'Artà (AR-09) at 3.5 ± 0.14 Ma that indicates a GMSL of 22.5 m.a.p.s.l. (11.3–25.7 m.a.p.s.l.).

Sample AR-03, with an inferred GMSL of 16.2 m.a.p.s.l. (5.6–19.2 m.a.p.s.l.) documents the youngest prominent Pliocene horizon in Coves d'Artà with an age of 3.27 ± 0.12 Ma (middle inset in Fig. 1d), which probably formed at the onset of the MPWP. If one accounts for GIA but assumes no long-term deformation, the GMSL during the MPWP is predicted to be 20.6 ± 2.8 m (Fig. 2). Overall, our calculations are most consistent with previous sea-level estimates that are based on benthic foraminifera^{10–12} (Fig. 3b). Our results are noticeably lower than the GMSL based on data by Rohling et al.² and higher than those based on ice-sheet modelling⁴ (Fig. 3b). The POS-based inferred GMSL for the MPWP is at the lower end of some previous estimates (25 ± 5 m and 22 ± 10 m)^{11,17} and overlaps with others (9–13.5 m)¹⁸.

The inherent uncertainties in predicting sea-level rise, when warming is triggered by future anthropogenic emissions of greenhouse gases, emphasize the importance of a better constraint on ice-sheet sensitivity to prolonged warming²⁷. The present-day East Antarctic Ice Sheet is less vulnerable to warming than the Greenland Ice Sheet

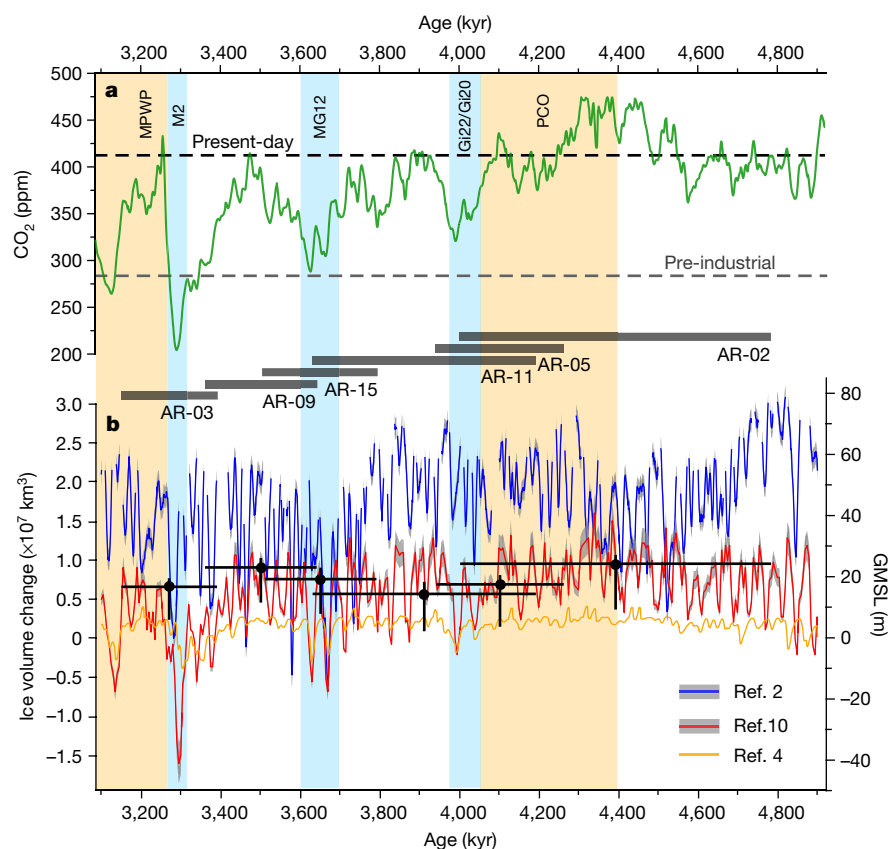


Fig. 3 | Pliocene sea-level and CO₂ concentration changes.

a, Model-based CO₂ reconstruction²¹ and relevant warm (orange bands) and cold (blue bands) climatic periods. **b**, Inferred GMSL and ice volume from Mallorcan POS are shown as black markers (age uncertainties are 2σ; the GMSL of the marker corresponds to the mode; uncertainties are 16th and 84th percentiles). The sample code for each POS is indicated on the grey band between panels. Coloured curves show three different GMSL reconstructions (uncertainties on GMSL curves are 1σ). See Methods for the derivation of the GMSL curves. PCO, Pliocene Climatic Optimum.

and the West Antarctic Ice Sheet²⁸. Considering this, the equivalent ice volume required for an MPWP GMSL of 16.2 m.a.p.s.l. (5.6–19.2 m.a.p.s.l.) (AR-03) would indicate a near or full collapse of the modern Greenland Ice Sheet (7.4 m GMSL rise)²⁹ and vulnerable sectors of the West Antarctic Ice Sheet (3.3 m GMSL rise)³⁰, plus a contribution of up to 5.5 m from more stable sectors of the West Antarctic Ice Sheet and from the East Antarctic Ice Sheet. Given that the marine sectors of the East Antarctic Ice Sheet hold an ice volume equivalent to 19 m of GMSL rise³¹, our estimates do not require a contribution from land-based sectors of the East Antarctic Ice Sheet. Instead, they indicate a possible retreat of East Antarctic Ice Sheet in some marine-based sectors, but stability of land-based ice masses, which is consistent with proxies from Antarctica^{26,32} and ice-sheet models⁷; we are thus able to narrow in on closing the sea-level budget for the MPWP.

Given that global average temperatures during the MPWP were 2–3 °C higher than pre-industrial values⁹ and CO₂ concentration was 400 ppm (ref. ⁹), our results indicate that an ice volume equivalent to a GMSL change of 16.2 m.a.p.s.l. (5.6–19.2 m.a.p.s.l.) may eventually melt (over hundreds to thousands of years) if future temperatures stabilize at that level of warming. Given present-day melt patterns²⁶, this sea-level rise is likely to be sourced from a collapse of both Greenland and the West Antarctic ice sheets. A temperature increase to 4 °C above pre-industrial levels is comparable to conditions during the Pliocene Climatic Optimum⁶ with a GMSL estimate of 23.5 m.a.p.s.l. (9.0–26.7 m.a.p.s.l.), which indicates further ice melt if temperatures stabilize at this higher level. Thermal expansion is expected to cause additional sea-level rise in these scenarios.

Projections of future sea-level rise that are tuned to fit the GMSL during the MPWP suggest that the Antarctic contribution to sea level by 2100 will be either 1.05 ± 0.30 m or 0.64 ± 0.49 m, if its GMSL contribution during the MPWP was assumed to be 10–20 m.a.p.s.l. or 5–15 m.a.p.s.l., respectively (under scenario RCP8.5)⁷. However, Edwards¹⁶ questioned the way marine ice cliff instability and hydrofracturing is parameterized in this work and found the latter interval to be more probable. Our AR-03-derived MPWP sea-level range (5.6–19.2 m.a.p.s.l.), which includes contributions from all ice sheets, is also more in line with the lower end of the estimates of DeConto and Pollard⁷. Nonetheless, this highlights (1) the need for further work to reduce uncertainty in MPWP GMSL estimates, and (2) the importance of our results for the even warmer Pliocene Climatic Optimum (9.0–26.7 m.a.p.s.l.). These data will serve as critical inputs for future climate model development and calibration that will improve confidence in sea-level projections. Hence, deciphering the GMSL during Pliocene warmth is critical for our ability to forecast, adapt to, and lessen the effect of future global warming on humanity.

Online content

Any methods, additional references, Nature Research reporting summaries, source data, extended data, supplementary information, acknowledgements, peer review information; details of author contributions and competing interests; and statements of data and code availability are available at <https://doi.org/10.1038/s41586-019-1543-2>.

Received: 8 January 2019; Accepted: 3 July 2019;

Published online 30 August 2019.

1. Dutton, A. et al. Sea-level rise due to polar ice-sheet mass loss during past warm periods. *Science* **349**, aaa4019 (2015).
2. Rohling, E. J. et al. Sea-level and deep-sea-temperature variability over the past 5.3 million years. *Nature* **508**, 477–482 (2014); corrigendum **510**, 432 (2014).
3. Raymo, M. E., Kozdon, R., Evans, D., Lisiecki, L. & Ford, H. L. The accuracy of mid-Pliocene $\delta^{18}\text{O}$ -based ice volume and sea level reconstructions. *Earth Sci. Rev.* **177**, 291–302 (2018).

4. De Boer, B., van de Wal, R. S. W., Bintanja, R., Lourens, L. J. & Tuerent, E. Cenozoic global ice-volume and temperature simulations with 1-D ice-sheet models forced by benthic $\delta^{18}\text{O}$ records. *Ann. Glaciol.* **51**, 23–33 (2010).
5. Haywood, A. M. et al. Large-scale features of Pliocene climate: results from the Pliocene Model Intercomparison Project. *Clim. Past* **9**, 191–209 (2013).
6. Fedorov, A. V. et al. Patterns and mechanisms of early Pliocene warmth. *Nature* **496**, 43–49 (2013).
7. DeConto, R. M. & Pollard, D. Contribution of Antarctica to past and future sea-level rise. *Nature* **531**, 591–597 (2016).
8. Zachos, J. C., Shackleton, N. J., Revenaugh, J. S., Palikey, H. & Flower, B. P. Climate response to orbital forcing across the Oligocene-Miocene boundary. *Science* **292**, 274–278 (2001).
9. Pagani, M., Liu, Z. H., LaRiviere, J. & Ravelo, A. C. High Earth-system climate sensitivity determined from Pliocene carbon dioxide concentrations. *Nat. Geosci.* **3**, 27–30 (2010).
10. Lisiecki, L. E. & Raymo, M. E. A Pliocene-Pleistocene stack of 57 globally distributed benthic $\delta^{18}\text{O}$ records. *Paleoceanography* **20**, PA1003 (2005).
11. Dwyer, G. S. & Chandler, M. A. Mid-Pliocene sea level and continental ice volume based on coupled benthic Mg/Ca palaeotemperatures and oxygen isotopes. *Phil. Trans. R. Soc. A* **367**, 157–168 (2009).
12. Naish, T. R. & Wilson, G. S. Constraints on the amplitude of Mid-Pliocene (3.6–2.4 Ma) eustatic sea-level fluctuations from the New Zealand shallow-marine sediment record. *Phil. Trans. R. Soc. A* **367**, 169–187 (2009).
13. Rovere, A. et al. The Mid-Pliocene sea-level conundrum: glacial isostasy, eustasy and dynamic topography. *Earth Planet. Sci. Lett.* **387**, 27–33 (2014).
14. Raymo, M. E., Mitrovica, J. X., O'Leary, M. J., DeConto, R. M. & Hearty, P. J. Departures from eustasy in Pliocene sea-level records. *Nat. Geosci.* **4**, 328–332 (2011).
15. Rowley, D. B. et al. Dynamic topography change of the Eastern United States since 3 million years ago. *Science* **340**, 1560–1563 (2013).
16. Edwards, T. L. et al. Revisiting Antarctic ice loss due to marine ice-cliff instability. *Nature* **566**, 58–64 (2019).
17. Miller, K. G. et al. High tide of the warm Pliocene: implications of global sea level for Antarctic deglaciation. *Geology* **40**, 407–410 (2012).
18. Winnick, M. J. & Caves, J. K. Oxygen isotope mass-balance constraints on Pliocene sea level and East Antarctic Ice Sheet stability. *Geology* **43**, 879–882 (2015).
19. Polyak, V. J. et al. A highly resolved record of relative sea level in the western Mediterranean Sea during the last interglacial period. *Nat. Geosci.* **11**, 860–864 (2018).
20. Kendall, R. A., Mitrovica, J. X. & Milne, G. A. On post-glacial sea level—II. Numerical formulation and comparative results on spherically symmetric models. *Geophys. J. Int.* **161**, 679–706 (2005).
21. Moucha, R. & Ruetenik, G. A. Interplay between dynamic topography and flexure along the U.S. Atlantic passive margin: insights from landscape evolution modeling. *Global Planet. Change* **149**, 72–78 (2017).
22. Stap, L. B. et al. CO₂ over the past 5 million years: continuous simulation and new $\delta^{13}\text{C}$ -based proxy data. *Earth Planet. Sci. Lett.* **439**, 1–10 (2016).
23. De Schepper, S., Gibbard, P. L., Salzmann, U. & Ehlers, J. A global synthesis of the marine and terrestrial evidence for glaciation during the Pliocene Epoch. *Earth Sci. Rev.* **135**, 83–102 (2014).
24. Passchier, S. Linkages between East Antarctic Ice Sheet extent and Southern Ocean temperatures based on a Pliocene high-resolution record of ice-rafted debris off Prydz Bay, East Antarctica. *Palaeoceanogr. Paleoclimatol.* **26**, PA4204 (2011).
25. Mudelsee, M. & Raymo, M. E. Slow dynamics of the Northern Hemisphere glaciation. *Paleoceanography* **20**, PA4022 (2005).
26. Williams, T. et al. Evidence for iceberg armadas from East Antarctica in the Southern Ocean during the late Miocene and early Pliocene. *Earth Planet. Sci. Lett.* **290**, 351–361 (2010).
27. Foster, G. L. & Rohling, E. J. Relationship between sea level and climate forcing by CO₂ on geological timescales. *Proc. Natl Acad. Sci. USA* **110**, 1209–1214 (2013).
28. Church, J. A. et al. Sea level change. *Climate Change 2013: The Physical Science Basis* (Cambridge Univ. Press, 2013).
29. Morlighem, M. et al. BedMachine v3: complete bed topography and ocean bathymetry mapping of Greenland from multibeam echo sounding combined with mass conservation. *Geophys. Res. Lett.* **44**, 11051–11061 (2017).
30. Bamber, J. L., Riva, R. E., Vermeersen, B. L. & LeBrocq, A. M. Reassessment of the potential sea-level rise from a collapse of the West Antarctic Ice Sheet. *Science* **324**, 901–903 (2009).
31. Fretwell, P. et al. Bedmap2: improved ice bed, surface and thickness datasets for Antarctica. *Cryosphere* **7**, 375–393 (2013).
32. Shakun, J. D. et al. Minimal East Antarctic Ice Sheet retreat onto land during the past eight million years. *Nature* **558**, 284–287 (2018).

Publisher's note Springer Nature remains neutral with regard to jurisdictional claims in published maps and institutional affiliations.

© The Author(s), under exclusive licence to Springer Nature Limited 2019

METHODS

POS as precise sea-level index points. POS are meaningful sea-level index points because they provide spatial geographic positioning, accurate elevation and absolute ages. In addition, the growth of POS has a clear indicative meaning, which includes the 'indicative range', that is, the elevation range over which a sea-level indicator forms, and the 'reference water level', meaning the distance between the sea-level indicator and sea level³³. The indicative range for POS is the vertical extent over which the carbonate encrustations occur and the reference water level is zero at the widest part of the POS (Extended Data Fig. 1). This is true because the widest part (maximum thickness) of the POS that formed on cave walls or other speleothems that are in continuous contact with the fluctuating water table corresponds to mean sea level, whereas the vertical spread constrains the tidal range (top and bottom insets in Fig. 1d). The shape of POS formed on pre-existing vadose (air-filled caves) speleothems depends on their size and morphology and for how long they were immersed in the cave's brackish water (Extended Data Fig. 1). If, for example, only the tip of the stalactites become submerged, the resulting POS will be an asymmetric knob-like carbonate encrustation with its thickest part denoting the mean sea level and narrowing upward to the highest tide range (see the asterisked POS in Extended Data Fig. 1). Thus, the most optimal POS form when the speleothem is immersed throughout the full vertical tidal range, producing an oval (sometimes spherical) or fusiform-shaped POS (middle inset in Fig. 1d, Extended Data Fig. 1a). Except for AR-02, which is a knob-like POS, all the others were either standalone (Extended Data Fig. 1a) or cave-wall (Extended Data Fig. 1b) structures.

Prior to our sampling campaign, a detailed topographic survey was conducted starting from a reference point outside the cave and situated at the present sea level, using a SUUNTO optical clinometer and a BOSCH DLE 50 Professional laser distance meter. The errors associated with measuring the elevation of the POS levels relative to the mean tidal level (after correcting for the barometric pressure) are less than 0.25 m. Owing to the large size of some POS horizons, cores were drilled using a commercial cordless hand-held Hilti rotary hammer drill.

U–Pb analytical methods. Absolute isotope-dilution U–Pb ages were measured using a Thermo Neptune multi-collector inductively coupled mass spectrometer. The analytical methodology is reported in Decker et al.³⁴. All sub-samples used for U–Pb measurements were clean, well crystallized aragonite or calcite pieces. A calibrated mixed ²²⁹Th–²³³U–²³⁶U–²⁰⁵Pb spike was used. The column chemistry for all of these analyses uses 1 × 8 chloride form 200–400 mesh anion resin. Each element isotope system was run separately. Pb runs were measured as standard-sample-standard runs using the Pb standard NBS-981. ²³⁴U signals too small to measure in the centre Faraday cup were measured using the secondary electron multiplier with the gain between the secondary electron multiplier and Faraday cups established using the U standard NBL-112. ²³⁰Th and ²³²Th were also measured using the secondary electron multiplier and a Faraday cup, respectively, and a Th in-house standard. ²³⁰Th/²³⁸U was measured to check samples for U and Th isotope secular equilibrium.

Age calculations. Reduction of data was performed using PBDAT³⁵ and ISOPLOT³⁶. Our measured procedural blanks are 5 pg of ²³²Th, <0.1 fg of ²³⁰Th, 20 pg of ²³⁸U, and ~15 pg of ²⁰⁸Pb. Decay constants for ²³⁸U, ²³⁵U, ²³⁴U and ²³⁰Th are from Schoene et al.³⁷ and Cheng et al.³⁸. The isotopic values for the NBS-981 Pb standard reported by the National Institute of Standards were used in the sample-standard method³⁹. U–Pb ages were corrected for initial disequilibrium assuming an initial ²³⁴U/²³⁸U activity of 1.75, based on the average initial ^δ²³⁴U of over 200 samples from the same island, ranging from Holocene to Pleistocene, dated using the U–Th method. Additionally, results of ^δ²³⁴U measurements of the present-day brackish water in which POS precipitate (as described earlier) indicate similar values¹⁹.

Except for AR-02, for which the ²³⁵U–²⁰⁷Pb two-dimensional isochron age was more favourable than the three-dimensional isochron ages, all other sample ages were calculated using the U–Pb Concordia-constrained linear three-dimensional isochron, which contains the most complete information on the concordance between the two decay schemes and common Pb (see Extended Data Fig. 2).

In certain plots, a limited number of discrepant data have been excluded from the fit, for reasons which are not under statistical control, such as non-uniform Pb composition and possibly variable initial ^δ²³⁴U. We excluded the subsamples that deviated markedly from the isochron lines in order to make sure that the isotopic analysis did not mix growth zones of domains with different ages. Considering that our samples precipitated in a phreatic environment, growth layers are hardly noticeable, so sampling along a single layer was challenging. Nevertheless, we stress that our analysed datasets are large enough to allow us to distinguish any discordant data, and as a result, the calculated ages are considered to be accurate within the given uncertainties. To have a superior control on the random uncertainties and for a better recognition of the outliers, we analysed between 9 and 15 subsamples for each isochron to obtain the ages, their uncertainties, and associated mean-square-weighted deviation values.

GIA modelling. For the GIA correction we adopt a one-dimensional, self-gravitating, Maxwell viscoelastic Earth model²⁰, which accounts for shoreline migration and the feedback into Earth's rotation axis. Following Raymo et al.¹⁴ we separate the GIA correction into two contributions: (1) the amount of residual deformation that is due to the most recent Pleistocene glacial cycles, and (2) the amount of deformation due to the smaller Pliocene ice age cycles. For both corrections we use a set of different Earth structure profiles that vary in lithospheric thickness (48 km, 71 km and 96 km), upper-mantle viscosity (3×10^{20} Pa s, 5×10^{20} Pa s), and lower-mantle viscosity (3×10^{21} Pa s, 5×10^{21} Pa s, 7×10^{21} Pa s, 10×10^{21} Pa s, 20×10^{21} Pa s and 30×10^{21} Pa s), producing 36 different radial viscosity profiles. For the elastic and density structure we assume the seismic reference model PREM⁴⁰. In this approach we neglect explicit three-dimensional variations in viscosity; although these unarguably exist, their pattern and magnitude are poorly constrained. Owing to these uncertainties and the high computational cost associated with these runs we follow the common approach to explore uncertainties in viscosity through a variety of one-dimensional viscosity profiles. We believe that this approach is particularly appropriate because we are not investigating spatial patterns in GIA (for which three-dimensional variability might be important), but focus on only one location.

For the two GIA contributors mentioned above we proceed as follows. (1) We adopt the ice history over the past 3 Myr as described in Raymo et al.¹⁴. The models indicate a positive GIA correction for most of the Mediterranean (Extended Data Fig. 3a), mainly due to ongoing peripheral bulge collapse associated with the former Fennoscandian Ice Sheet. This sea-level rise implies that Coves d'Artà is currently above its equilibrium sea level and that sea-level indicators that formed during the more equilibrated Pliocene need to be corrected downward. Using one possible viscoelastic Earth model (Extended Data Fig. 3a) indicates that the remaining adjustment at Coves d'Artà is 3.4 m. Employing all 36 model runs yield a mean and standard deviation of 4.5 ± 2.1 m for this location (Extended Data Fig. 3).

(2) We constructed new ice models by scaling the height of present-day ice sheets to reproduce a given ice-volume curve. We set up three different ice models based on the LR04 benthic stack¹⁰, the local sea-level reconstructions by Rohling et al.², and the ice-sheet model by de Boer et al.⁴. Uncertainties will be assessed by considering these three ice models rather than propagating uncertainties in each of them. However, we acknowledge that large uncertainties exist for each approach and these will be considered in the long-term deformation component (see Methods section 'Estimating long-term deformation'). The ice-volume curves are constructed for each model as follows.

(1) To scale the oxygen isotope signal into ice-volume changes, we assume that 75% of the signal is driven by ice volume (the remaining 25% is driven by temperature variations). This value is in line with Pleistocene ocean temperature estimates obtained using Mg/Ca ratio^{17,41}. We further assume a scaling of 0.011‰ per metre of GMSL rise^{3,12}.

(2) Rohling et al.² used planktonic foraminifera and the marginal basin residence time method for the Mediterranean to produce a relative sea-level record for the Strait of Gibraltar (RSLGib_{observed}). They further provide a scaling to calculate ice volume (GMSL_{scaled} = $1.23 \times \text{RSLGib}_{\text{observed}} + 0.5$), which is based on simulations for two glacial cycles. We use this scaling as a first estimate for ice-volume changes. We next run the sea-level model to calculate local sea-level changes at the Strait of Gibraltar for a variety of viscosity models. We take the mean of these local sea-level estimates (RSLGib_{calculated}) to calculate a GIA correction (GIA = RSLGib_{calculated} – GMSL_{scaled}). Last, we use this correction to recalculate the GMSL estimate (GMSL = RSLGib_{observed} – GIA). We note that the original sea-level reconstruction has data gaps associated with the African monsoon. We use the interpolated reconstruction here, but exclude data during these gaps in our final comparison (Fig. 3).

(3) De Boer et al.⁴ used a set of one-dimensional ice-sheet simulations that are forced by a benthic oxygen isotope record through surface-air temperatures. They separately model five ice sheets (Greenland Ice Sheet, Laurentide, Fennoscandian, West Antarctic Ice Sheet and East Antarctic Ice Sheet) and provide an ice-volume reconstruction over the Cenozoic.

For times during which ice volume was lower than today, we first decrease the height of the Greenland Ice Sheet and West Antarctic Ice Sheet until they are fully collapsed before we start decreasing the height of the East Antarctic Ice Sheet. For ice volumes higher than today we uniformly increase the size of all ice sheets. Ice-rafted debris and other evidence from the Greenland continental shelf indicates that an intermittent ice sheet existed on Greenland during the Pliocene, but that the main expansion probably happened around 3 Ma (ref. 42). This is largely consistent with our ice reconstructions based on the GMSL scenarios described above. We further tested a scenario in which only the Antarctic Ice Sheet varied over the model run and the Greenland Ice Sheet was not present. This introduced only minor differences (<0.6 m) in the GIA correction at Coves d'Artà and is therefore not considered further here.

Calculations were done with a temporal resolution of 1,000 years and a spatial resolution up to spherical harmonic degree 256. The GMSL throughout the paper is directly proportional to total ice volume (not only ice above flotation) given by the equation:

$$\text{GMSL} = \frac{\text{Ice volume changes} \times \rho_{\text{ice}}}{\text{Percentage oceanic area} \times \rho_{\text{water}}}$$

For the percentage oceanic area we use a fixed value of 71.1% and further use a water density of $1,000 \text{ kg m}^{-3}$ and an ice density of 920 kg m^{-3} .

The resulting GMSL and local sea-level curve for Coves d'Artà for one run is shown in the Extended Data Fig. 4a along with a snapshot of sea level at 3.244 Ma (Extended Data Fig. 4b). Local sea level (coloured curves) is lower than the GMSL (black curves) during times when ice sheets were collapsed. This difference is driven by the accommodation space that is created by the collapsed marine-based sectors. Water flowing back to these areas causes high rates of sea-level rise (for example, in West Antarctica), which is averaged out by an overall drawdown in sea level in the far field (Extended Data Fig. 4a). These runs are relative to the start of the model time (outside the range shown in Extended Data Fig. 4b), which was set to be the present-day ice configuration.

The full GIA correction is given by a combination of both effects described above. The resulting local sea-level prediction is shown in Extended Data Fig. 5. Our calculations show that local sea level tracks the GMSL relatively closely when the GMSL is high (Extended Data Fig. 5a) because the two contributions discussed above cancel out. When the GMSL is low (Extended Data Fig. 5c) the GIA signal is mainly driven by the ongoing adjustment to the Last Glacial Maximum, which means the GIA correction is positive (Extended Data Fig. 3; Extended Data Fig. 5f).

The GIA correction is given by the difference between the local sea level at Coves d'Artà and the GMSL ($\text{GIA} = \text{RSL}_{\text{Artà calculated}} - \text{GMSL}$). To quantify the GIA correction and its uncertainty for each POS we take a temporal average and standard deviation of all GIA models (using all three GMSL curves) over the time period of the sea-level indicators. We consider only corrections during intermediate and warm periods, assuming that these provide more favourable conditions for POS to form. This assumption is based on the fact that POS form during sea-level still stands and the Pleistocene still stands occur more frequently during intermediate and warm periods than during glacial⁴³. Weakening this assumption would lead to a slightly larger uncertainty in the GIA correction. To include this assumption, we identify the GMSL values (and their associated GIA correction) that fall within the age range of each POS, and average over the GIA correction that corresponds to the highest 50% of GMSL values (80% in the case of AR-03 to avoid a bias towards MIS M2, Extended Data Fig. 5). We combine values from the three ice models to calculate the mean and standard deviation in the GIA correction for each data point (Table 1).

Estimating long-term deformation. Mallorca is generally described as stable with very little to no long-term deformation^{44,45}. However, even a small amount of deformation (uplift or subsidence) can substantially affect our results. We therefore investigate constraints on the long-term deformation of the island based on sea-level records from other time periods. We further attempt to quantify uncertainties on the possible amount of uplift by comparing the relative elevations of the six POS to the relative GMSL change in the three curves described above^{2,12}.

POS in Mallorca that date to MIS 5a are above present sea level today⁴⁶. The GIA correction for this location is small and the GMSL was possibly around present levels but probably lower⁴⁷, indicating potential uplift. POS dated to the last interglacial are found at $2.15 \pm 0.75 \text{ m.a.p.s.l.}$ ¹⁹. Given the uncertainties in the eustatic estimate during the last interglacial and the GIA correction, it is difficult to identify uplift or subsidence. Late Miocene reefs that crop out at 65 m above present at Cap Blanc⁴⁸ and up to 70 m in the hinterland of Mallorca^{44,49} are also high compared to global average values (once corrected for GIA), but Late Miocene GMSL estimates are much more uncertain⁵⁰. Given that local sea-level estimates tend to be high, it is unlikely that subsidence occurred at Coves d'Artà. We will therefore assume that the record presented here is not affected by subsidence; however, the evidence reported above does not exclude slight long-term uplift.

We estimate the amount of possible long-term uplift based on relative sea-level changes across the POS record and its comparison to the three GMSL reconstructions. Unlike our GIA calculation, uncertainties in the different GMSL curves will be important for this analysis and we therefore choose the following approach to quantify the respective uncertainties.

(1) For the GMSL curve that is obtained from the LR04 benthic record¹⁰ we widen the range for scaling oxygen isotope values into GMSL change to 0.008 and 0.011‰ per metre^{3,17} to produce two end-member GMSL curves. We assume that the mean of these two curves is the most likely estimate, and the two end-member curves constitute 1σ uncertainty. This results in a wider uncertainty than if we only assumed that the two end-members would span the range of possible GMSL curves. This extended uncertainty is meant to implicitly include further

uncertainties associated with estimating the amount of oxygen isotope signal that is driven by ice volume versus temperature.

(2) The GMSL curve based on the data by Rohling et al.² is obtained through the equation $\text{GMSL} = \text{RSL}_{\text{Gib observed}} - \text{GIA}$, excluding the gaps in their planktonic foraminiferal dataset due to maxima in the African monsoon. We calculate the uncertainty at each timestep as the root mean square of the uncertainty associated with the relative sea-level observation (provided by Rohling et al.²) and the uncertainty associated with the GIA correction for the Strait of Gibraltar that is caused by varying viscosity models.

(3) De Boer et al.⁴ do not quantify an uncertainty in their estimate, so we do not show it in Fig. 3. However, for our long-term deformation analysis we do want to attempt an uncertainty estimate. De Boer et al.⁴ do two sensitivity tests in which they vary the deep-water to surface-air temperature coupling, and the temperature difference for the Northern Hemisphere ice sheets. They found that their predicted ice volume was relatively insensitive to these variations with a largest difference between runs of $\sim 3.5 \text{ m}$ during the Pliocene. Here we assume that their best-fit curve represents a mean estimate and that the 1σ uncertainty is 1 m.

While the GMSL reconstructions described above and shown in Fig. 3 vary widely, relative changes, for example, the change in GMSL from the Pliocene Climatic Optimum to the MPWP could be more robust. We quantify bounds on the amount of sea-level change that occurred between the different POS from our three GMSL reconstructions. For each reconstruction we generate 500 possible GMSL curves, sampling the uncertainty in each of them (grey bands in Extended Data Fig. 6a–c are 1σ). We next bin the GMSL values that fall within the age range of each POS and identify values that are within a certain (average to high) percentile range to reflect intermediate and warm periods. For the purpose of calculating an uplift rate we again assume that it is more likely that these are the periods during which our POS formed. We vary the lower bound between the 40th, 50th and 60th percentiles and the upper bound between the 90th, 95th and 99th percentiles. Extended Data Fig. 6a–c shows the range of GMSL values considered for each POS as grey boxes for a scenario of the 50th percentile lower bound and 99th percentile upper bound. We do a Monte Carlo simulation in which we randomly sample 'synthetic' sea-level indicator elevations from the respective GMSL ranges, that is, we pick one random point from each grey box in Extended Data Fig. 6a–c. We next calculate the change in sea level in these synthetic data relative to the youngest data point. These changes are compared to the observed changes in sea level (GIA corrected) to which we add a constant uplift rate. We choose this uplift rate to be constant, but vary its magnitude in each iteration. This assumes that long-term deformation is linear to first order over the Plio-Pleistocene, which is supported by studies of mantle convection that show that uplift rates related to dynamic topography are relatively constant over a few million years⁵¹. We consider the synthetic data to be a good fit to the observed data if their difference does not exceed 3 m for a given data point. This value is chosen because it is the root mean square of the average GIA uncertainty, the measurement uncertainty, and half the indicative range. We record the uplift rates that are successful, that is, produce a good fit.

Extended Data Fig. 6d–f shows histograms of these successful uplift rates for a scenario of 50th percentile lower bound and 99th percentile upper bound. GMSL curves that are based on Rohling et al.² and the LR04 benthic record¹⁰ favour small uplift rates, because the variability within these curves is already large enough to represent the variability within the POS elevation data. However, there is a tail towards higher uplift rates. The GMSL curve based on de Boer et al.⁴ is notably flatter and, in order to match the elevation variability in the POS results, these data require a modest amount of uplift. We produce a joint distribution, in which we combine all successful uplift rates (Extended Data Fig. 6g). We repeat this procedure varying the lower-bound and upper-bound percentiles as described above to obtain nine joint distributions (Extended Data Fig. 7a–i). Last, we combine the successful uplift rates from all nine joint distributions to obtain our final distribution, which is the basis for our long-term uplift correction (Extended Data Fig. 7j). The median uplift rate that we obtain is 2.0 m Myr^{-1} ($0.6\text{--}4.4 \text{ m Myr}^{-1}$; uncertainties constitute the 16th and 84th percentiles). The most likely uplift rate (highest number of successful runs) is 0 m Myr^{-1} . These rates are within the uncertainty range of uplift estimates for Mallorca based on the MIS 5e sea-level estimate⁵².

Correcting local sea level to obtain the GMSL. We produce a probability density function (PDF) for the elevation of each POS. We first take into account the uncertainty of the measurement (0.25 m) and the indicative meaning (half the indicative range). Since we assume that these errors are normally distributed, the resulting PDF (blue curve, Fig. 2c) is also normally distributed. We next correct for GIA assuming the values shown in Extended Data Fig. 5, which results in the red curve (Fig. 2c). In the next step, we account for thermal expansion. We assume a linearly increasing effect of thermal expansion, $0.39 \text{ m of GMSL rise per degree Celsius}^{53}$ and 4°C of warming at the beginning of the Pliocene Climatic Optimum ($4.4\text{--}4.0 \text{ Ma}$)⁶. To calculate the thermal expansion correction from this rate we require the age of each POS. We randomly sample the age of the POS from its uncertainty range. This correction is again normally distributed, resulting in a new PDF that is

normally distributed as well (yellow curve, Fig. 2c). Last, we account for long-term deformation. We use the distribution that we obtain as described above (Extended Data Fig. 7j) for this correction. We sample the age of the POS again to translate an uplift rate into the amount of total uplift. The resulting PDF (purple curve, Fig. 2c) is off-centred owing to the skewness in the long-term deformation distribution. We therefore do not quantify uncertainties as standard deviations but instead determine the mode (most likely value) as our preferred value (GMSL) and the 16th and 84th percentiles as error bounds. We use a kernel with 1-m bandwidth to calculate the mode. Extended Data Fig. 8 shows the PDFs for the GMSL estimate for each POS after all corrections have been applied. Extended Data Table 1 includes additional percentiles of the GMSL estimate (10th, 33th, 50th, 66th and 90th) in line with IPCC's likelihood scale.

Data availability

The data produced in this study are available at the NOAA (<https://www.ncdc.noaa.gov/paleo/study/27530>) and Pangaea (<https://doi.pangaea.de/10.1594/PANGAEA.905851>) data repositories.

Code availability

The computer code used to do the sea-level (GIA) calculation, written in MATLAB, is available on github: <https://github.com/jaustermann/SLcode>.

33. Rovere, A. et al. The analysis of Last Interglacial (MIS 5e) relative sea-level indicators: reconstructing sea-level in a warmer world. *Earth Sci. Rev.* **159**, 404–427 (2016).
34. Decker, D. D. et al. U–Pb dating of cave spar: a new shallow crust landscape evolution tool. *Tectonics* **37**, 208–223 (2018).
35. Ludwig, K. R. & Titterton, D. M. Calculation of $^{230}\text{Th}/\text{U}$ isochrons, ages, and errors. *Geochim. Cosmochim. Acta* **58**, 5031–5042 (1994).
36. Ludwig, K. R. *User's Manual for Isoplot 3.75: A Geochronological Toolkit for Microsoft Excel* http://www.bgc.org/isoplot_etc/isoplot/isoplot3_75-4_15manual.pdf (Berkeley Geochronology Center Special Publication 5, 2012).
37. Schoene, B. et al. Reassessing the uranium decay constants for geochronology using ID-TIMS U–Pb data. *Geochim. Cosmochim. Acta* **70**, 426–445 (2006).
38. Cheng, H. et al. Improvements in ^{230}Th dating, ^{230}Th and ^{234}U half-life values, and U–Th isotopic measurements by multi-collector inductively coupled plasma mass spectrometry. *Earth Planet. Sci. Lett.* **371–372**, 82–91 (2013).
39. Yuan, H. et al. Evaluation of lead isotope compositions of NIST NBS 981 measured by thermal ionization mass spectrometer and multiple-collector inductively coupled plasma mass spectrometer. *Solid Earth Sci.* **1**, 74–78 (2016).
40. Dziewonski, A. M. & Anderson, D. L. Preliminary reference Earth model. *Phys. Earth Planet. Inter.* **25**, 297–356 (1981).
41. Elderfield, H. et al. Evolution of ocean temperature and ice volume through the Mid-Pleistocene Climate Transition. *Science* **337**, 704–709 (2012).
42. Bierman, P. R., Shakun, J. D., Corbett, L. B., Zimmerman, S. R. & Rood, D. H. A persistent and dynamic East Greenland Ice Sheet over the past 7.5 million years. *Nature* **540**, 256–260 (2016).
43. Shakun, J. D., Lea, D. W., Lisiecki, L. E. & Raymo, M. E. An 800-kyr record of global surface ocean $\delta^{18}\text{O}$ and implications for ice volume-temperature coupling. *Earth Planet. Sci. Lett.* **426**, 58–68 (2015).
44. Pomar, L. & Ward, W. C. in *Sequence Stratigraphy and Depositional Response to Eustatic, Tectonic and Climatic Forcing* (ed. Haq, B. U.) Ch. 4, 87–112 (Kluwer, 1995).
45. Just, J., Hübscher, C., Betzler, C., Lüdmann, T. & Reicherter, K. Erosion of continental margins in the Western Mediterranean due to sea-level stagnancy during the Messinian Salinity Crisis. *Geo-Mar. Lett.* **31**, 51–64 (2011).
46. Dorale, J. A. et al. Sea-level highstand 81,000 years ago in Mallorca. *Science* **327**, 860–863 (2010).
47. Creveling, J. R., Mitrovica, J. X., Clark, P. U., Waelbroeck, C. & Pico, T. Predicted bounds on peak global mean sea level during marine isotope stages 5a and 5c. *Quat. Sci. Rev.* **163**, 193–208 (2017).
48. Pomar, L. Reef geometries, erosion surfaces and high-frequency sea-level changes, upper Miocene Reef Complex, Mallorca, Spain. *Sedimentology* **38**, 243–269 (1991).
49. Pomar, L. La evolución tectonosedimentaria de las Baleares: análisis crítico. *Acta Geol. Hisp.* **14**, 293–310 (1979).
50. Miller, K. G. et al. The Phanerozoic record of global sea-level change. *Science* **310**, 1293–1298 (2005).
51. Flament, N. et al. A review of observations and models of dynamic topography. *Lithosphere* **5**, 189–210 (2013).
52. Stocchi, P. et al. MIS 5e relative sea-level changes in the Mediterranean Sea: contribution of isostatic disequilibrium. *Quat. Sci. Rev.* **185**, 122–134 (2018).
53. Meehl, G. A. et al. *Climate Change 2007: The Physical Science Basis* (Cambridge Univ. Press, 2007).

Acknowledgements We thank the owner and personnel of Coves d'Artà for granting permission and offering logistic support during the field research conducted for this study. We thank F. L. Forray and G. Lucia for helping with the coring process. B.P.O. and V.J.P. are funded by a collaborative NSF grant (AGS 1602670). Additional research costs were covered by a NSF grant (EAR 0326902 to Y.A. and V.J.P.) and MINECO grants (CGL2013-48441-P and CGL2016-79246-P to J.J.F.). O.A.D. received student research grants from the Cave Research Foundation, the Geological Society of America, and the Fred L. and Helen M. Tharp Endowed Scholarship (School of Geosciences, University of South Florida). J.A. thanks the PALSEA working group and the NSF (grant OCE-0825293 “PLIOMAX”) for facilitating discussions at regular meetings, and the Vetlesen Foundation for support.

Author contributions B.P.O., J.J.F. and O.A.D. designed the research. A.G. and J.G. first documented the presence of POS in the cave studied. B.P.O., J.J.F., J.G., A.G. and O.A.D. measured POS elevations and collected samples. V.J.P., O.A.D. and Y.A. measured U–Pb ages of POS samples. J.A. produced the GIA and long-term deformation corrections. O.A.D., J.A. and B.P.O. drafted and wrote the majority of the manuscript with input from all authors.

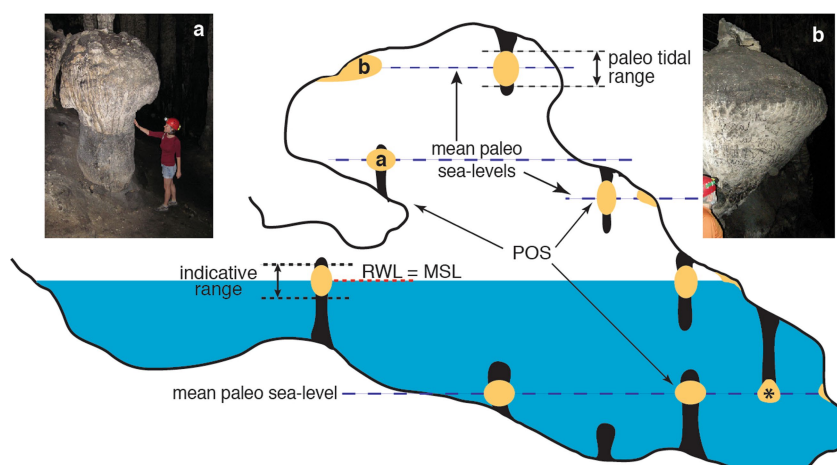
Competing interests The authors declare no competing interests.

Additional information

Correspondence and requests for materials should be addressed to B.P.O.

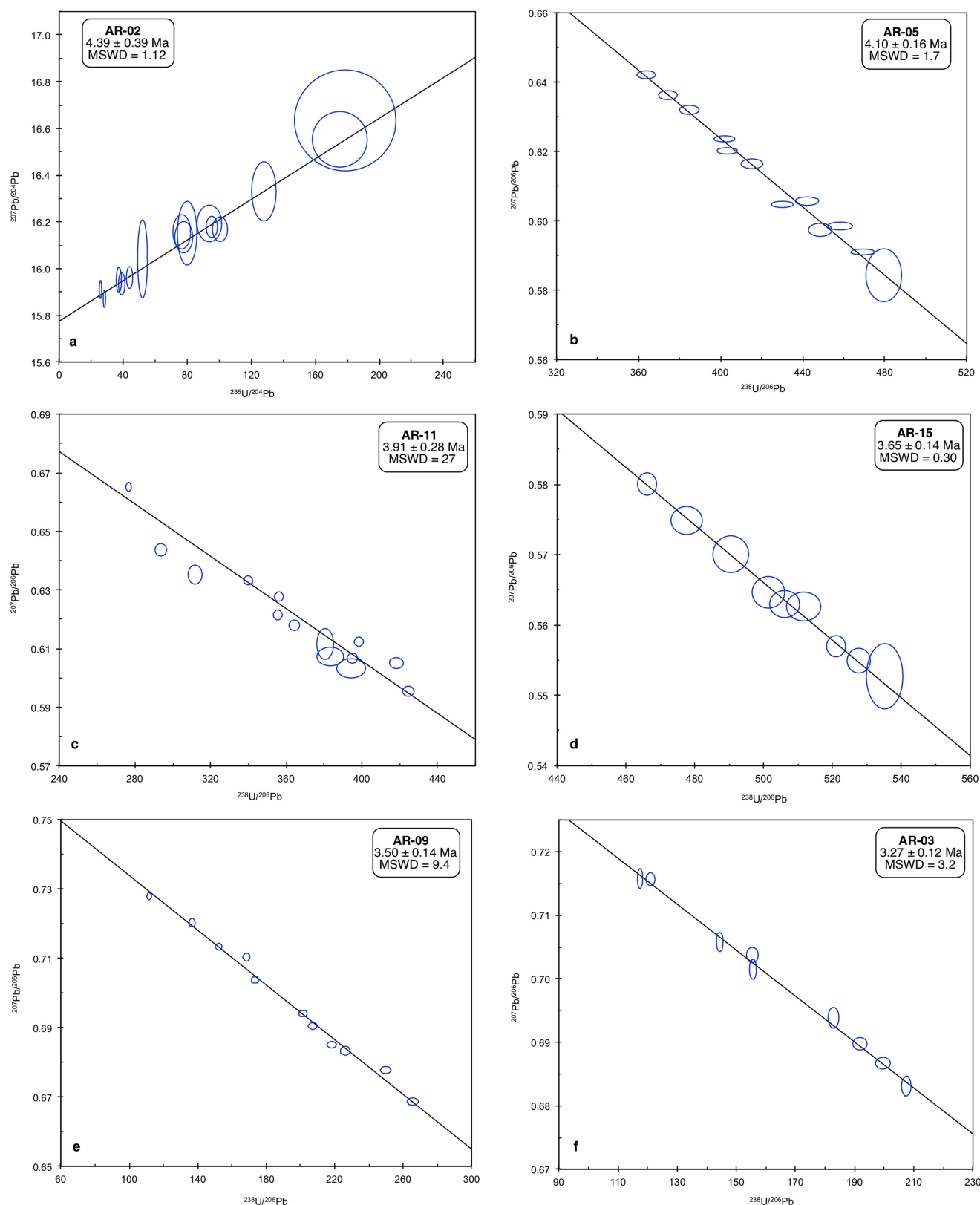
Peer review information *Nature* thanks Eelco Rohling, Jon Woodhead and the other, anonymous, reviewer(s) for their contribution to the peer review of this work.

Reprints and permissions information is available at <http://www.nature.com/reprints>.



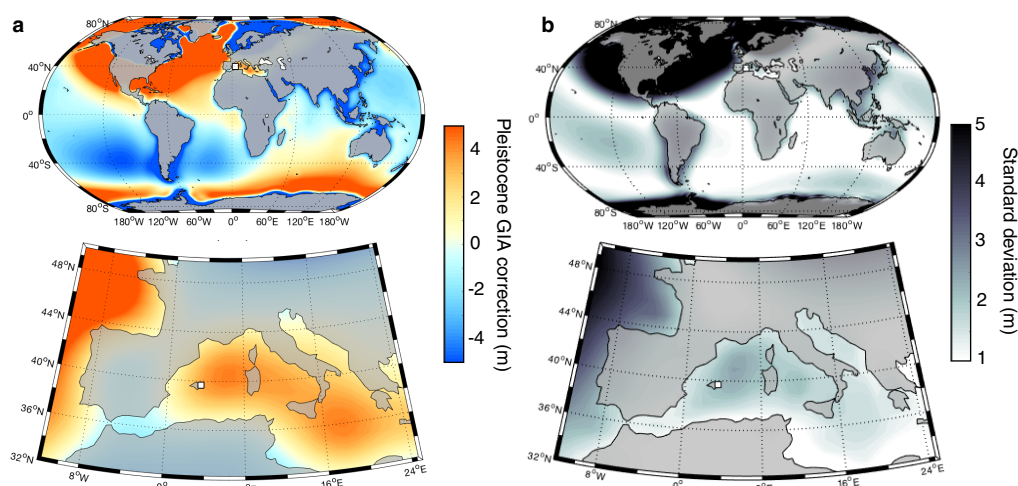
Extended Data Fig. 1 | Schematic profile of a coastal cave in Mallorca hosting POS at different levels. a, b, Standalone (a) and cave-wall (b) POS structures. The asterisk POS is an example of an asymmetric knob-

like carbonate encrustation that forms when only the tip of the stalactite is submerged.



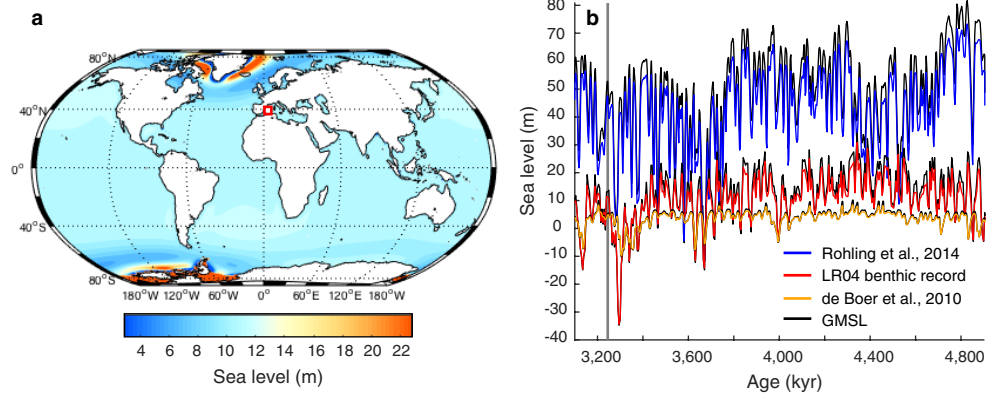
Extended Data Fig. 2 | U-Pb isochron and calculated age estimates for the six POS samples. a, ^{235}U - ^{207}Pb two-dimensional isochron for sample AR-02; **b-f,** Concordia-constrained linear three-dimensional isochron for

samples AR-05 (**b**), AR-11 (**c**), AR-15 (**d**), AR-09 (**e**) and AR-03 (**f**). Error ellipses on individual ages are 2σ .



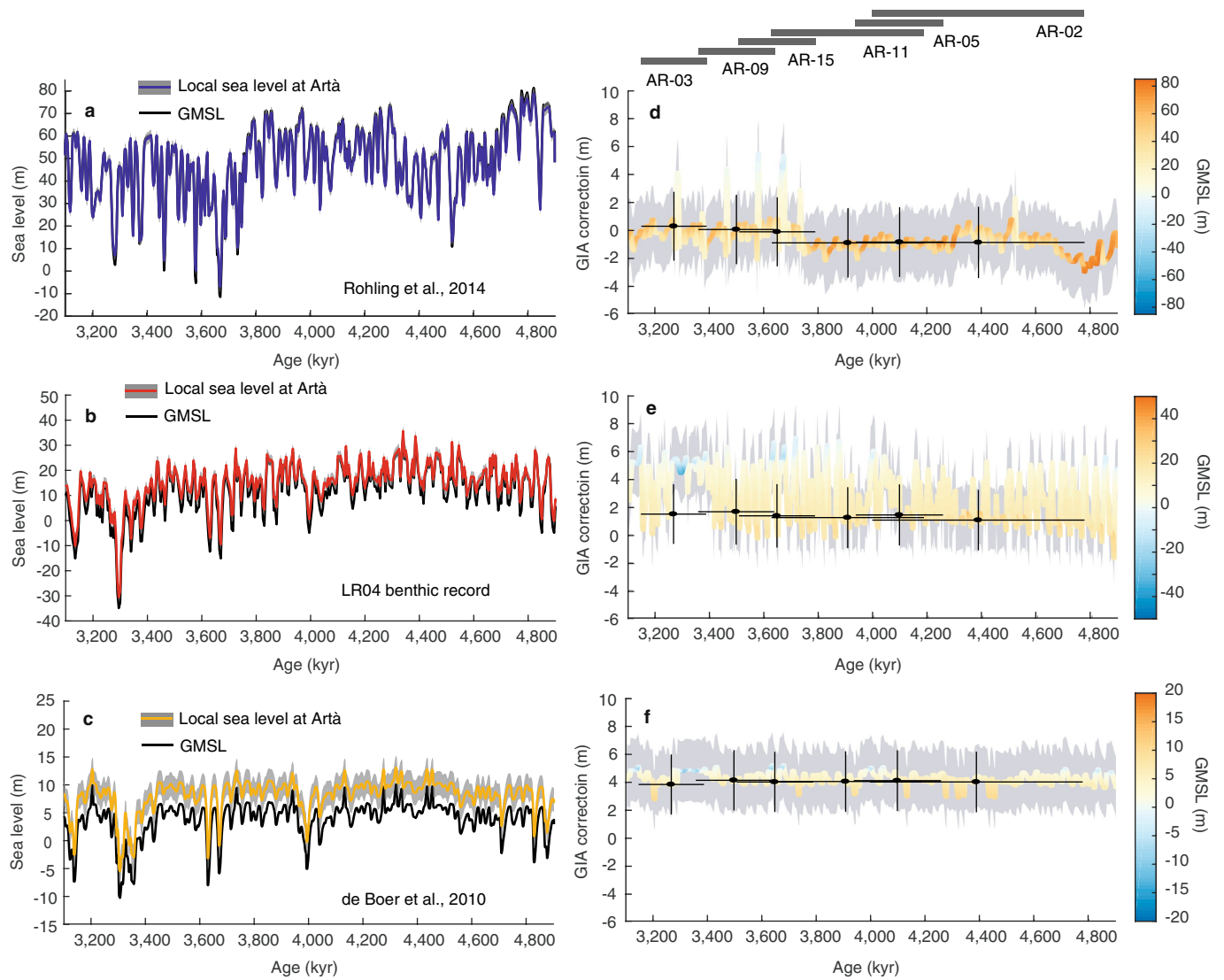
Extended Data Fig. 3 | GIA contribution due to ongoing adjustment. This GIA contribution is caused by the incomplete present-day adjustment to the late Pleistocene ice and ocean loading cycles. **a**, Model simulation using a viscosity structure of 5×10^{20} Pa s viscosity in the upper mantle, 5×10^{21} Pa s viscosity in the lower mantle, and an elastic lithospheric

thickness of 96 km. **b**, Standard deviation of model predictions obtained using 36 different radial viscosity profiles, including varying the lithospheric thickness. The square marks the position of Coves d'Artà. The figures were produced using Matlab 2015b and the `m_map` plotting package (<https://www.eoas.ubc.ca/~rich/map.html>).



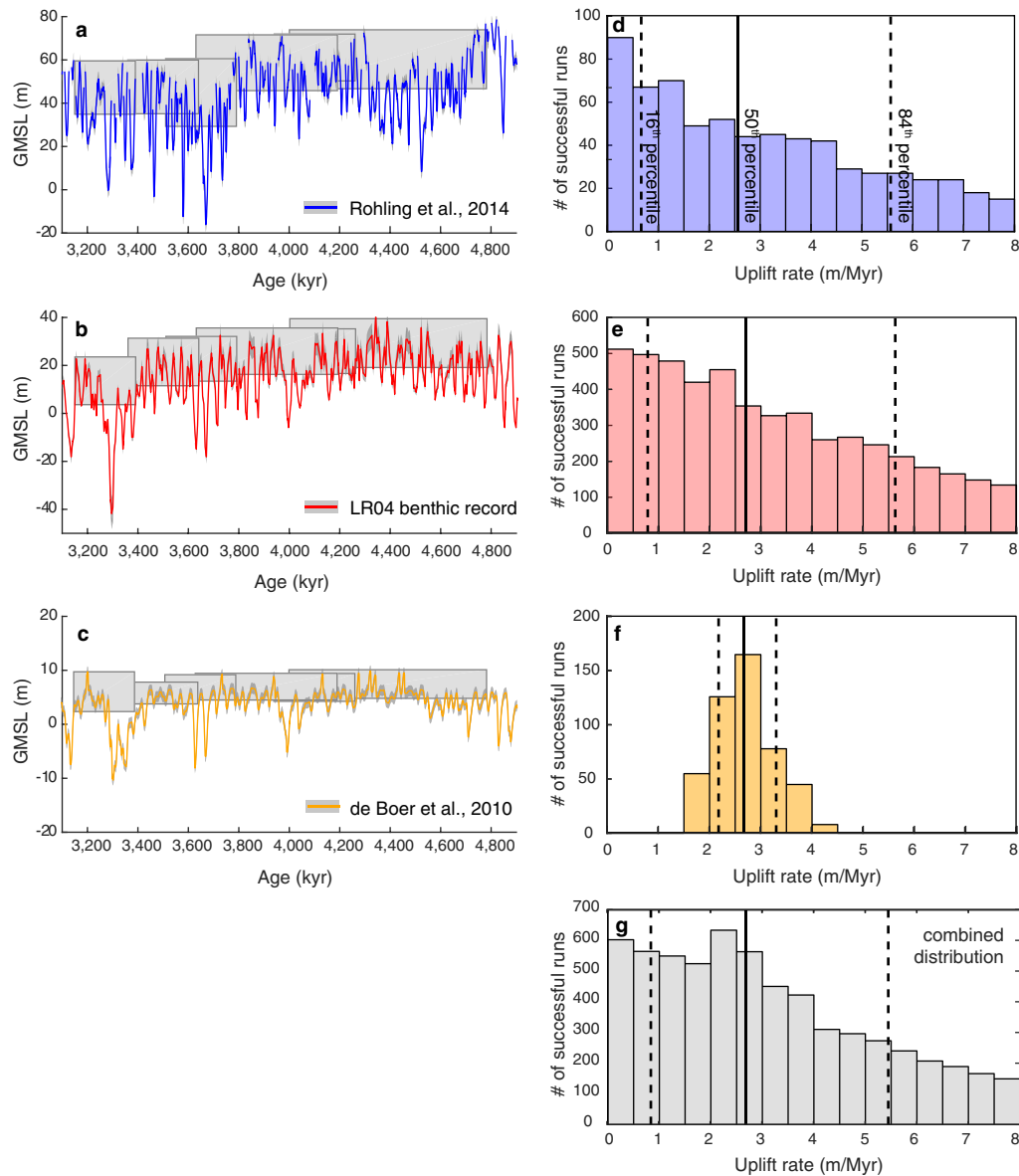
Extended Data Fig. 4 | GIA contribution due to Pliocene ice age cycles. The model simulation uses a viscosity structure of 5×10^{20} Pa s viscosity in the upper mantle, 5×10^{21} Pa s viscosity in the lower mantle, and an elastic lithospheric thickness of 96 km. **a**, Snapshot of sea level at 3.244 Ma (grey vertical line in **b**) assuming a GMSL curve based on the LR04 benthic record¹⁰. The colour scale is chosen to diverge around the GMSL value of 13 m. The red square marks the position of Coves d'Artà. The figure was produced using Matlab 2015b and the `m_map` plotting package

(<https://www.eoas.ubc.ca/~rich/map.html>). **b**, Local sea level at Coves d'Artà based on Rohling et al.² (blue), de Boer et al.⁴ (yellow), and the LR04 benthic record¹⁰ (red). Respective GMSL curves are shown in black and mostly coincide with local sea level at Coves d'Artà (note that for the estimates based on Rohling et al.² the black GMSL curve is mostly behind the local sea-level curve in blue). Sea level is relative to the beginning of this run (4.9 Ma).



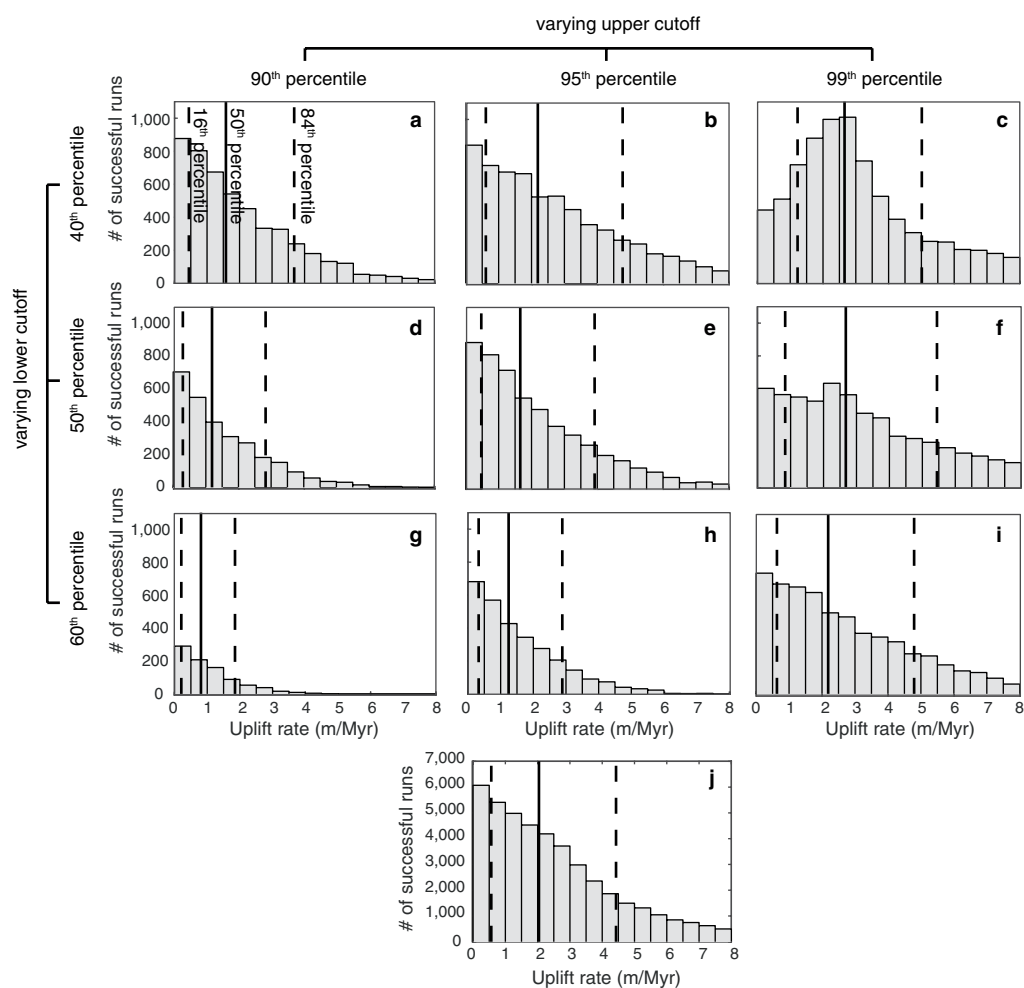
Extended Data Fig. 5 | Total GIA correction. a–c, Local sea-level change at Coves d'Artà, as calculated from the GIA model based on the GMSL curves by Rohling et al.² (a), the LR04 benthic record¹⁰ (b) and de Boer et al.⁴ (c). Uncertainties due to Earth's viscoelastic structure are denoted by grey bands. d–f, GIA correction colour coded by the GMSL value;

standard deviations are shown as grey bands. Black markers indicate the GIA correction and its uncertainty for each POS. Results are for the GMSL curves by Rohling et al.² (d), the LR04 benthic record¹⁰ (e) and de Boer et al.⁴ (f).



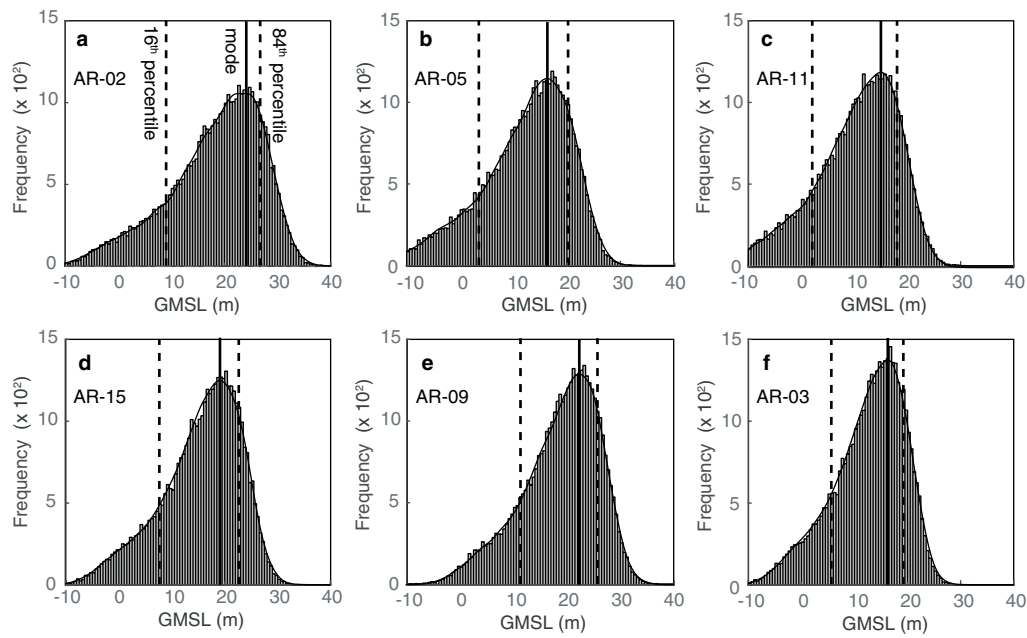
Extended Data Fig. 6 | Uplift rate estimation. Determining the amount of uplift based on the best fit of observed relative sea-level changes across the POS to other GMSL reconstructions over the same time interval. **a–c**, GMSL curves^{2,4,10}; grey bars are 1σ uncertainties. Boxes indicate the age uncertainty for each POS and the 50th and 99th percentiles of the GMSL values that fall within this age range. We calculate synthetic sea-level changes relative to the youngest POS and compare them

to the observed sea-level changes, assuming a range of uplift rates. **d–f**, Histograms of uplift rates in which we find a good fit between the observed and the synthetic data. Percentiles (16th, 50th and 84th) are shown by vertical lines (solid line is the median, dashed lines are uncertainty bounds). We conducted ten million iterations for this Monte Carlo search. **g**, Histogram combining all uplift rates that resulted in a good fit.



Extended Data Fig. 7 | Joint uplift rate estimation from varying the upper and lower cutoff. a–i, Joint histograms for a variety of lower and upper percentile cutoffs. The lower cutoff was varied between the 40th, 50th and 60th percentiles (different rows), whereas the upper cutoff was varied between the 90th, 95th and 99th percentiles (different columns).

Percentiles in the histograms (16th, 50th and 84th) are shown by vertical lines (solid line is the median, dashed lines are uncertainty bounds). Panel f is identical to Extended Data Fig. 6g. j, Combination of all joint histograms to obtain our best-estimate uplift rate used for Table 1, Fig. 2c and Fig. 3.



Extended Data Fig. 8 | Reconstructed elevation of the GMSL for each POS after all corrections have been applied. a–f, PDFs for the GMSL estimate for AR-02, AR-05, AR-11, AR-15, AR-09 and AR-03, respectively. PDFs are constructed assuming Gaussian uncertainties for the measured elevation of POS, the respective indicative range, the GIA correction, thermal expansion and POS age (Table 1); a non-Gaussian distribution is

obtained for the uplift correction (Table 1, Extended Data Figs. 6, 7). The mode (thick black line) and lower and upper uncertainty bounds (16th and 84th percentiles, thick dashed lines) are shown by vertical lines and correspond to the GMSL estimates reported in Table 1. We used a kernel with 1-m bandwidth to calculate the mode and PDF (thin black line).

Extended Data Table 1 | GMSL estimates for different percentiles (10th, 33th, 50th, 66th and 90th) following IPCC's likelihood scale

Sample code	Age (Myr)	GMSL (m)					GMSL without correction for thermal expansion (m)				
		10 th	33 th	50 th	66 th	90 th	10 th	33 th	50 th	66 th	90 th
AR-02	4.39 ± 0.39	5.3	15.5	19.8	23.1	28.2	6.9	17.1	21.4	24.7	29.8
AR-05	4.10 ± 0.16	0.1	9.5	13.6	16.7	21.7	1.6	11.0	15.1	18.2	23.2
AR-11	3.91 ± 0.28	-1.3	7.8	11.6	14.6	19.5	0.1	9.2	13.0	16.0	20.9
AR-15	3.65 ± 0.14	4.5	13.1	16.6	19.4	24.0	5.8	14.4	17.9	20.7	25.3
AR-09	3.50 ± 0.14	8.2	16.5	19.9	22.6	27.0	9.4	17.7	21.1	23.8	28.2
AR-03	3.27 ± 0.12	2.9	10.5	13.7	16.3	20.4	4.1	11.7	14.9	17.5	21.6